Geochemistry Geophysics Geosystems G3
AN ELECTRONIC JOURNAL OF THE EARTH SCIENCES
Published by AGU and the Geochemical Society

Article
Volume 11, Number 3
12 March 2010
Q03S20, doi:10.1029/2009GC002841
ISSN: 1525-2027

Click Here for Full Article

Constraints on upper plate deformation in the Nicaraguan subduction zone from earthquake relocation and directivity analysis

S. W. French
Department of Geological Sciences, Brown University, 324 Brook Street, Box 1846, Providence, Rhode Island 02912, USA

Now at Berkeley Seismological Laboratory, University of California, Berkeley, California 94720, USA (sfrench@seismo.berkeley.edu)

L. M. Warren
National Science Foundation, 4201 Wilson Boulevard, Room 785N, Arlington, Virginia 22230, USA

Also at Department of Geosciences, University of Arizona, 1040 East 4th Street, Tucson, Arizona 85721, USA

K. M. Fischer
Department of Geological Sciences, Brown University, 324 Brook Street, Box 1846, Providence, Rhode Island 02912, USA

G. A. Abers
Lamont-Doherty Earth Observatory, PO Box 1000, 61 Route 9W, Palisades, New York 10964, USA

W. Strauch
Department of Geophysics, Instituto Nicaragüense de Estudios Territoriales, Apartado 2110, Managua, Nicaragua

J. M. Protti and V. Gonzalez
Observatorio Vulcanológico y Sismológico de Costa Rica, Universidad Nacional, Apartado 2346-3000, Heredia, Costa Rica

[1] In the Nicaraguan segment of the Central American subduction zone, bookshelf faulting has been proposed as the dominant style of Caribbean plate deformation in response to oblique subduction of the Cocos plate. A key element of this model is left-lateral motion on arc-normal strike-slip faults. On 3 August 2005, a M_w 6.3 earthquake and its extensive foreshock and aftershock sequence occurred near Ometepe Island in Lake Nicaragua. To determine the fault plane that ruptured in the main shock, we relocated main shock, foreshock, and aftershock hypocenters and analyzed main shock source directivity using waveforms from the TUCAN Broadband Seismic Experiment. The relocation analysis was carried out by applying the hypoDD double-difference method to *P* and *S* onset times and differential traveltimes for event pairs determined by waveform cross correlation. The relocated hypocenters define a roughly vertical plane of seismicity with an N60°E strike. This plane aligns with one of the two nodal planes of the main shock source mechanism. The directivity analysis was based on waveforms from 16 TUCAN stations and indicates that rupture on the N60°E striking main shock nodal plane provides the best fit to the data.

Copyright 2010 by the American Geophysical Union

The relocation and directivity analyses identify the N60°E vertical nodal plane as the main shock fault plane, consistent with the style of faulting required by the bookshelf model. Relocated hypocenters also define a second fault plane that lies to the south of the main shock fault plane with a strike of N350°E–N355°E. This fault plane became seismically active 5 h after the main shock, suggesting the influence of stresses transferred from the main shock fault plane. The August 2005 earthquake sequence was preceded by a small eruption of a nearby volcano, Concepción, on 28 July 2005. However, the local seismicity does not provide evidence for earthquake triggering of the eruption or eruption triggering of the main shock through crustal stress transfer.

Components: 9978 words, 9 figures, 1 table.

Keywords: earthquake relocation; fore-arc deformation; Central America; earthquake directivity; Nicaragua.

Index Terms: 7230 Seismology: Seismicity and tectonics (1207); 7240 Seismology: Subduction zones (1207); 8104 Tectonophysics: Continental margins: convergent.

Received 17 September 2009; **Revised** 2 December 2009; **Accepted** 17 December 2009; **Published** 12 March 2010.

French, S. W., L. M. Warren, K. M. Fischer, G. A. Abers, W. Strauch, J. M. Protti, and V. Gonzalez (2010), Constraints on upper plate deformation in the Nicaraguan subduction zone from earthquake relocation and directivity analysis, *Geochem. Geophys. Geosyst.*, *11*, Q03S20, doi:10.1029/2009GC002841.

Theme: Central American Subduction System
Guest Editors: G. Alvarado, K. Hoernle, and E. Silver

1. Introduction

[2] In the Central American subduction zone, the Cocos plate subducts beneath the Caribbean plate at rates varying from 73 to 85 (±5) mm/yr, with a component of motion parallel to the trench [*McCaffrey*, 1996; *DeMets*, 2001]. From the Nicoya Peninsula in northern Costa Rica to El Salvador, a sliver of the Caribbean plate fore arc is translating to the northwest at rates of 6–15 mm/yr, based on geodetic data from the upper plate [*Lundgren et al.*, 1999; *Norabuena et al.*, 2004; *Iinuma et al.*, 2004; *Turner et al.*, 2007; *LaFemina et al.*, 2009] with the most recent estimate at 8–9 mm/yr [*LaFemina et al.*, 2009]. Fore-arc sliver transport has been interpreted as an outcome of oblique subduction [*McCaffrey*, 1996; *LaFemina et al.*, 2002; *Turner et al.*, 2007] and/or lateral escape of the upper plate lithosphere in response to upper plate shortening in southern Costa Rica associated with subduction of the buoyant Cocos Ridge [*LaFemina et al.*, 2009]. *Phipps Morgan et al.* [2008] propose that fore-arc sliver motion has occurred in the context of 3–10 mm/yr of arc-normal extension. Based on fault offsets imaged in Lakes Nicaragua and Managua, *Funk et al.* [2009] conclude that the Nicaraguan Depression (the low-lying region containing the lakes) (Figure 1) formed as a half-graben during past extension.

[3] In Nicaragua, competing models have been proposed for the mechanism that accommodates fore-arc sliver transport [*LaFemina et al.*, 2002; *Funk et al.*, 2009]. In the bookshelf faulting model [*LaFemina et al.*, 2002], upper plate blocks separated by NE striking left-lateral strike-slip faults rotate clockwise about vertical axes. This style of deformation contrasts with subduction zones where fore-arc sliver motion occurs by displacement on arc-parallel strike-slip faults within the upper plate, for example Sumatra, the Philippines and the Aleutians [e.g., *Fitch*, 1972; *Ekström and Engdahl*, 1989; *McCaffrey*, 1992; *McCaffrey et al.*, 2000; *Sieh and Natawidjaja*, 2000]. Recently however, *Funk et al.* [2009] concluded that fore-arc sliver transport in Nicaragua is primarily accommodated by right-lateral strike slip motion on a system of arc-parallel (NW striking) faults, including strike-slip overprinting of NW striking normal faults that previously allowed arc-normal extension.

[4] In Nicaragua, the source mechanisms of upper plate earthquakes are predominantly strike-slip and are consistent with both left-lateral motion on roughly vertical NE striking fault planes, or right-lateral motion on NW striking fault planes [*White*, 1991; *LaFemina et al.*, 2002, 2004]. However, *LaFemina et al.* [2002] favor bookshelf faulting over a zone of dextral arc-parallel shear, primarily

15252027, 2010, 3, Downloaded from https://agupubs.onlinelibrary.wiley.com/doi/10.1029/2009GC002841 by Cochrane Costa Rica, Wiley Online Library on [21/07/2025]. See the Terms and Conditions (https://onlinelibrary.wiley.com/terms-and-conditions) on Wiley Online Library for rules of use; OA articles are governed by the applicable Creative Commons License

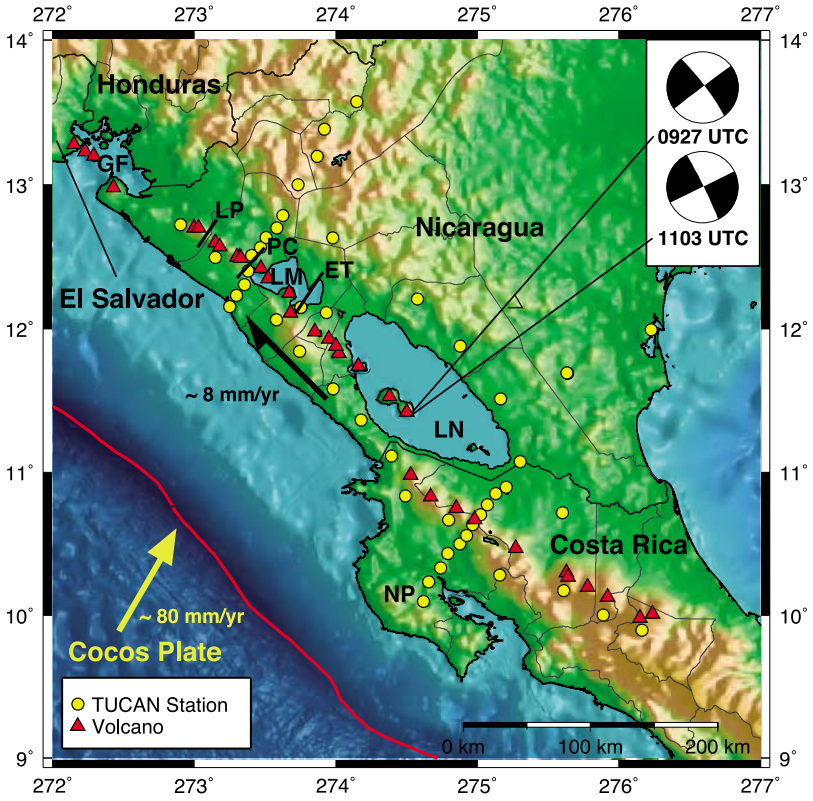

Figure 1. Overview of the study area. Arrows and labels indicate sense and rate of oblique subduction along the Cocos-Caribbean convergent margin and NW directed motion in the Nicaraguan fore arc. The heavy black lines in the northern Nicaraguan fore arc approximate the locations of documented NE striking left-lateral faulting; ET represents the Estadio and Tiscapa Faults, PC is the La Paz Centro fault zone, and LP is the La Pelona fault zone. Also shown are the moment tensor solutions for the 3 August 2005 M_w 5.3 foreshock and M_w 6.3 main shock (Global Centroid Moment Tensor Catalog, http://www.globalcmt.org), occurring at 0927 and 1103 UTC, respectively, and the locations of TUCAN broadband stations (yellow circles) and arc volcanoes (red triangles). Lake Nicaragua (LN), Lake Managua (LM), the Gulf of Fonseca (GF), and the Nicoya Peninsula (NP) are labeled.

because geologically mapped NE striking fault zones cut across the arc in a number of regions. Some of these zones have been the locus of significant earthquakes, most notably the destructive Managua earthquakes of 1931 and 1972 [*Carr and Stoiber*, 1977; *Weinberg*, 1992; *van Wyk de Vries*, 1993; *Cowan et al.*, 2000; *LaFemina et al.*, 2002]. This correlation may be due, at least in part, to rheological variations between weaker crust beneath volcanic centers and the stronger adjacent crust in which the NE striking fault zones lie; these strength contrasts could elevate stress and promote failure within the arc-normal fault zones [*Cailleau et al.*, 2007]. The best documented examples of NE striking faults across the arc are the Estadio and Tiscapa faults that cut through Managua, and two zones further along the arc to the northwest, the La Paz Centro fault zone and the La Pelona fault zone [*Weinberg*, 1992; *van Wyk de Vries*, 1993; *Cowan et al.*, 2000; *LaFemina et al.*, 2002, 2004; *Díez et al.*, 2005] (Figure 1). NE trending fault zones have also been inferred more broadly along the Nicaraguan arc [*Carr and Stoiber*, 1977; *LaFemina et al.*, 2002], but in these locations the seismological and geological evidence for the faults and their sense of motion is less clear. In contrast, *Funk et al.* [2009] prefer arc-parallel shearing over bookshelf faulting as the mechanism of fore-arc sliver transport because they did not observe regular, parallel left-lateral strike-slip faults in Lakes Nicaragua and Managua that extend well beyond the volcanic front.

[5] To the north, fore-arc sliver transport in El Salvador is thought to occur as right-lateral motion on an arc-parallel shear zone [*Martínez-Díaz et al.*, 2004; *Funk et al.*, 2009]. In the Costa Rican arc to the south, *Marshall et al.* [2000] have mapped both NE striking left-lateral faults and NW striking right-lateral faults, but indicate that the longer NW striking (arc-parallel) faults are the dominant structures. For example, a M_w 6.2 earthquake with

15252027, 2010, 3, Downloaded from https://agupubs.onlinelibrary.wiley.com/doi/10.1029/2009GC002841 by Cochrane Costa Rica, Wiley Online Library on [21/07/2025]. See the Terms and Conditions (https://onlinelibrary.wiley.com/terms-and-conditions) on Wiley Online Library for rules of use; OA articles are governed by the applicable Creative Commons License

a fault plane striking NW to NNW occurred 30 km NNW of San José in January 2009 [*Red Sismológica Nacional*, 2009; J. Pacheco, personal communication, 2009].

[6] Left-lateral motion on roughly NE trending faults is a cornerstone of the bookshelf faulting model [*LaFemina et al.*, 2002]. A recent earthquake sequence in Lake Nicaragua offers the opportunity to test for the existence of left-lateral roughly NE trending strike-slip faults in a region of the arc in which such structures have been proposed by some studies [*Carr and Stoiber*, 1977; *LaFemina et al.*, 2002], but not observed in others [*Funk et al.*, 2009]. On 3 August 2005, a magnitude M_w 5.3 event occurred at 0927 UTC near Ometepe Island in Lake Nicaragua, followed by a magnitude M_w 6.3 event at 1103 UTC. Moment tensor solutions for these events (Global Centroid Moment Tensor Catalog, http://www.globalcmt.org) [*Ekström*, 2007] are typical of arc earthquakes and are consistent with left-lateral strike-slip motion along a N64°E trending vertical plane or right-lateral strike-slip motion along a N334°E trending vertical plane (Figure 1). These events were followed by a cluster of hundreds of smaller, but detectable, events over the next three weeks (Instituto Nicaragüense de Estudios Territoriales (INETER) Monthly Earthquake Catalog, http://www.ineter.gob.ni). However, while these events were all initially located within 40 km of the initial main shock location, their spatial distribution was too diffuse to delineate a rupture plane and distinguish between the N64°E and N334°E fault planes that are consistent with the main shock source mechanism.

[7] The primary goal of this study was to determine the rupture plane of the 3 August 2005, M_w 6.3 earthquake, in order to shed light upon patterns of faulting in southern Nicaragua. The fault plane was delineated using two approaches: double-difference relocation of the earthquakes in the August 2005 sequence using the hypoDD method developed by *Waldhauser and Ellsworth* [2000], and analysis of directivity in the main shock source with the approach of *Warren and Silver* [2006]. These analyses were applied to data from the TUCAN (Tomography Under Costa Rica and Nicaragua) Broadband Seismometer Experiment, a temporary array of broadband seismometers that was in the field from July 2004 to March 2006 (yellow circles in Figure 1). TUCAN stations provided more complete sampling in event-station azimuth and distance than was possible with the stations of the INETER network and the two permanent seismic networks in Costa Rica, one run by the Observatorio Vulcanológico y Sismológico de Costa Rica (OVSICORI) at the Universidad Nacional and the other by the Universidad de Costa Rica and the Instituto Costarricense de Electricidad. In addition, most permanent stations in the region were short period, and the broadband data collected with the TUCAN array facilitated the directivity analysis.

[8] Another interesting facet of this earthquake sequence was that it was preceded by a small eruption of Concepción, the northwest of the two volcanoes comprising Ometepe Island in Lake Nicaragua (Figure 1), on 28 July 2005 (Smithsonian Institution Global Volcanism Program, http://www.volcano.si.edu). A period of minor eruptive activity continued until 10 November 2005. Triggering of volcanism by tectonic earthquakes has been observed elsewhere in the Nicaraguan arc [*White and Harlow*, 1993; *LaFemina et al.*, 2004; *Díez et al.*, 2005], but these few cases appear to be the exception to a general lack of temporal correlation between major earthquakes and eruptions over the last century [*White and Harlow*, 1993]. Unambiguous examples of deformation and stress transfer from a specific volcanic eruption triggering a significant tectonic earthquake have not been documented in this region, although they have been inferred in other locations globally [e.g., *Nostro et al.*, 1998]. The 16 December 1985 M_w 6.1 earthquake, which occurred along the Ochomogo fault zone at the northern end of Lake Nicaragua [*LaFemina et al.*, 2002], was also preceded by the onset of a period of eruptive activity at Concepción, lasting from roughly 2 December 1985 through 20 April 1986 (Smithsonian Institution Global Volcanism Program, http://www.volcano.si.edu); however, no direct causal link has yet been established. Thus, a secondary goal of this study is to explore the relationship of the 2005 Lake Nicaragua earthquake sequence to the 2005 Concepción eruption.

2. Relocation Method

[9] Double-difference relocation [*Waldhauser and Ellsworth*, 2000] was applied to earthquakes in the INETER catalog for the months of July and August 2005, specifically the 296 events shallower than 40 km that fell within a 0.5° × 0.5° box centered on the catalog location of the 3 August 2005, main shock. Data used in the relocation were absolute *P* and *S* arrival times and differential cross-correlation times obtained from waveforms recorded by the stations of the TUCAN array.

15252027, 2010, 3, Downloaded from https://agupubs.onlinelibrary.wiley.com/doi/10.1029/2009GC002841 by Cochrane Costa Rica, Wiley Online Library on [21/07/2025]. See the Terms and Conditions (https://onlinelibrary.wiley.com/terms-and-conditions) on Wiley Online Library for rules of use; OA articles are governed by the applicable Creative Commons License

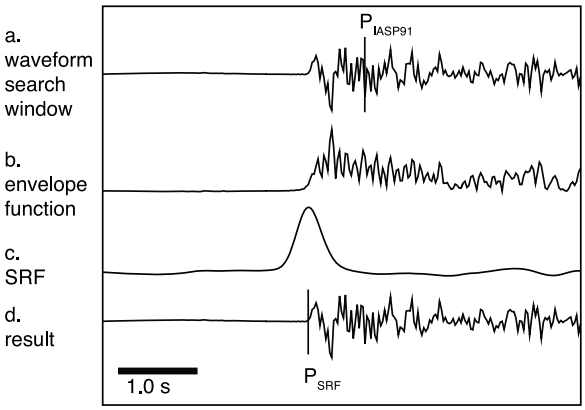

Figure 2. An illustration of automated phase arrival picking, similar to that proposed by *Earle and Shearer* [1994]. (a) The waveform search window, containing the IASP91-predicted phase arrival. (b) Associated envelope function and (c) resulting smoothed ratio function (SRF). (d) The phase arrival corresponding to the SRF maximum.

2.1. Automated Phase Picking

[10] Automated phase picking was employed to generate a catalog of *P* and *S* phase arrivals at all 48 TUCAN stations for the 296 events of interest. We identified phase onset times using a short-term average/long-term average (STA/LTA) ratio function of the phase amplitude similar to the approach of *Earle and Shearer* [1994]. *P* times were measured from vertical components and *S* times from transverse components. We sampled 10 s windows of TUCAN waveform data centered on *P* and *S* onset times predicted from the IASP91 reference earth model (Figure 2a), over which we calculated envelope functions, thus yielding measurements of absolute amplitude (Figure 2b). The STA/LTA ratio function is a comparison of average absolute amplitude in a long window (0.6 s for *P*/1.0 s for *S*) characterizing the background "noise" immediately preceding and a short window (0.2 s for *P* and *S*) characterizing the current "signal" for some comparison time, resulting in an instantaneous estimate of signal-to-noise ratio. Ratio functions were calculated for all candidate phase windows and smoothed with a 0.2 s half-width Hann window, leading to the smoothed ratio function (SRF (Figure 2c)). A phase arrival corresponds to a rapid increase and local maximum in signal-to-noise ratio and thus also in the ratio function. While other choices are possible, we found that picking the peak of the local maximum in the ratio function provides a good analog for a phase pick (Figures 2c and 2d). The amplitude of this peak also conveys information regarding the impulsiveness of the arrival and the quality of the pick.

[11] We manually checked a random sample of the automated picks, and determined that the hand-picked and automated times agreed to within a few samples (±0.1 s) for 90% of the phases for ratio function peak amplitudes greater than 4.0 for *P* arrivals and 3.5 for *S* arrivals. Picks corresponding to lower ratio function amplitudes were discarded. With these thresholds, the application of the automated picking to the TUCAN data set for our entire event sequence resulted in 1686 *P* phase arrivals (from 13,345 windows tested) and 1950 *S* phase arrivals (from 13,240 windows tested). Most intermediate-magnitude events, including the M_w 5.3 foreshock, generated waveforms that performed well under the automated picking scheme. However, the M_w 6.3 main shock produced emergent *P* and *S* arrivals, and waveforms at several stations were clipped. For this event, *P* and *S* onset times were picked by hand.

2.2. Automated Waveform Cross Correlation

[12] Waveforms were sampled in 2 s windows centered on the *P* and *S* onset times determined by SRF (Figure 3, right) and band-pass filtered between 0.2 and 5 Hz. For each event pair and phase, cross correlograms were computed from waveform samples recorded at a common station (Figure 3, left). The peak amplitude and time offset of the discrete cross-correlation function were determined to subsample precision through application of polynomial curve fitting. In order to generate a cross-correlation differential traveltime, the time offset of the peak of the cross-correlation function was simply added to the difference of the phase onset times for the event pair, from which the difference in event origin times was then subtracted. Cross-correlation times were retained only if the peak value of the cross-correlation function was 0.8 or greater.

2.3. Double-Difference Relocation With hypoDD

[13] By operating on differences in traveltime to a common station for event pairs, double-difference relocation is able to achieve greater accuracy in interevent relative location. In particular, for two events much closer to each other than to a given station, their paths to the station will be very similar. By differencing traveltimes for suitable pairs of

15252027, 2010, 3, Downloaded from https://agupubs.onlinelibrary.wiley.com/doi/10.1029/2009GC002841 by Cochrane Costa Rica, Wiley Online Library on [21/07/2025]. See the Terms and Conditions (https://onlinelibrary.wiley.com/terms-and-conditions) on Wiley Online Library for rules of use; OA articles are governed by the applicable Creative Commons License

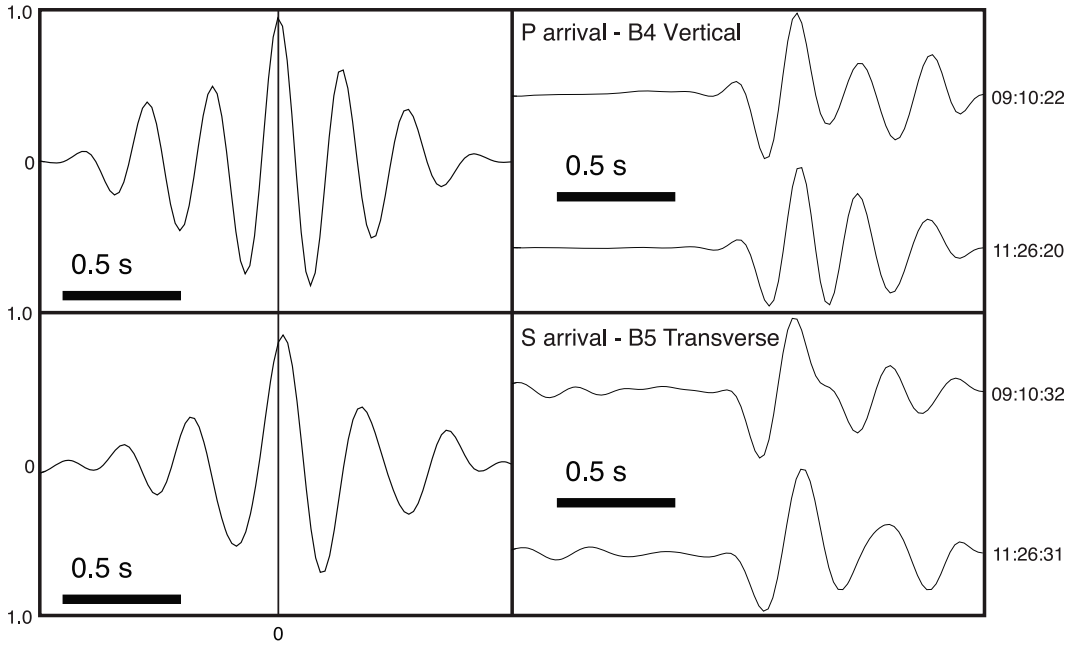

Figure 3. An illustration of waveform cross correlation of *P* and *S* phase arrivals for an arbitrary event pair. (top right) *P* arrivals recorded on the vertical component at TUCAN station B4 (windows beginning at 0910:22 and 1126:20 UTC) and (bottom right) *S* arrivals recorded on the transverse-rotated component at station B5 (windows beginning at 0910:32 and 1126:31). Both events were on 5 August 2005. (left) Cross correlograms of the waveform pairs shown in Figure 3 (right) for which the subsample peak offset time picks, determined as discussed in section 2.2, are +0.00398 and +0.019400 s for *P* and *S*, respectively.

events, uncertainty due to structure is reduced and a pairwise network of events can be relocated relative to each other to high accuracy [e.g., *Waldhauser and Ellsworth*, 2000; *Lin and Shearer*, 2005].

[14] The hypoDD method [*Waldhauser and Ellsworth*, 2000; *Waldhauser*, 2001] was employed to carry out the double-difference relocation. This code solves the double-difference equations using a damped least squares approach, and, given the number of events in our data set, we chose the conjugate gradient iterative solution method (LSQR) [*Paige and Saunders*, 1982]. Heavier damping was applied in early iterations when the solution was less stable, in particular to avoid relocation of these shallow events to negative depths (above ground). Damping was relaxed in later iterations (Table 1). A one-dimensional regional *P* wave model developed by INETER for routine event location in their permanent network was employed as a velocity model (Figure 4).

[15] Individual differential traveltime data were weighted to reflect confidence in each measurement. Differential times obtained from waveform cross correlation were weighted by the absolute value of their cross-correlation coefficient and the differential times obtained by differencing phase onset times were weighted by a [0,1] value that depended on the signal-to-noise ratios of the two automated onset time picks. An a priori weighting

Table 1. Damping and Weighting Parameters for Our Featured Double-Difference Relocation Using hypoDD[a]

NITER	WCCP	WCCS	WRCC	WDCC	WCTP	WCTS	WRCT	WDCT	DAMP
2	0.01	0.01	*	*	1.0	1.0	*	*	120
2	0.5	0.5	*	*	1.0	1.0	*	*	110
6	0.5	0.5	*	*	1.0	1.0	*	*	85
6	0.5	0.5	8 σ	10 km	0.8	0.8	8 σ	10 km	70
14	0.5	0.5	6 σ	10 km	0.5	0.5	6 σ	10 km	60

[a]*Waldhauser and Ellsworth* [2000] and *Waldhauser* [2001]. Shown are number of iterations (NITER), a priori weights for P and S cross correlation (WCCP and WCCS) and onset pick (WCTP and WCTS) differential traveltime data, dynamic cutoff for removal of outlier data (WRCC and WRCT), dynamic cutoff for removal of event pairs of large interevent separation (WDCC and WDCT), and finally damping parameter for the LSQR scheme (DAMP). Asterisk indicates no weighting applied.

15252027, 2010, 3, Downloaded from https://agupubs.onlinelibrary.wiley.com/doi/10.1029/2009GC002841 by Cochrane Costa Rica, Wiley Online Library on [21/07/2025]. See the Terms and Conditions (https://onlinelibrary.wiley.com/terms-and-conditions) on Wiley Online Library for rules of use; OA articles are governed by the applicable Creative Commons License

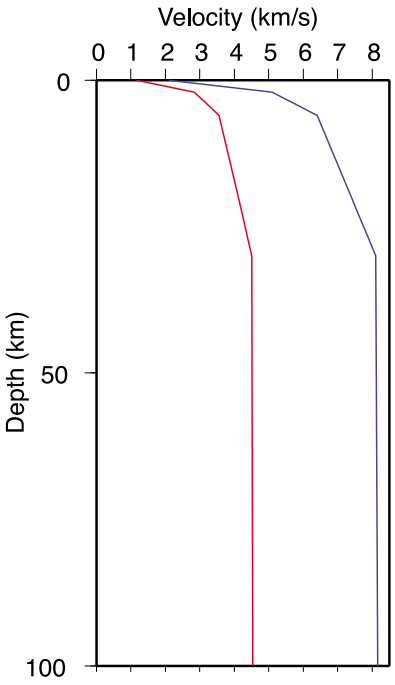

Figure 4. Regional velocity model used in this study, similar to that used by INETER for local event hypocenter determination. The *P* velocity model (blue) is a linearly interpolated version of that used by INETER, while the *S* velocity model (red) was determined for a regional constant V_P/V_S ratio of 1.80.

was used to control the influence of cross-correlation times versus phase picks and varied between iterations (Table 1). Dynamic weighting was used to remove differential traveltime data classified as outlier or corresponding to interevent distances greater than 10 km as the relocation progressed. If the initial hypocenter model is poor, and thus inconsistent with the data set, premature introduction of dynamic weighting may lead to erroneously discarded data. The weighting scheme employed in the relocation solution shown here (Table 1) aims to avoid this effect and was designed such that a priori–only weighting during the initial 10 iterations would bring the event hypocenters into general agreement with the data, while the latter 20 iterations would improve solution resolution with the introduction of dynamic weighting. Before arriving at the chosen data weighting and damping parameters (Table 1) a wide variety of values were tested. The general structure characterized by our featured solution persists regardless of perturbation to these parameters.

[16] The choice of initial event locations had more impact on the relocation. We chose to employ individual initial locations for each event, as opposed to a common location at the centroid of the event cluster [*Waldhauser and Ellsworth*, 2000]. In early relocation efforts, we simply employed hypocenters from the INETER catalog. However, some INETER catalog hypocenters were sufficiently inconsistent with the differential traveltime data from the TUCAN stations that stable networks of event pairs could not be formed. For example, a stable location for the main shock could not be found. We therefore formed a new initial location model in two steps. TUCAN array P and S traveltimes for the main shock were used to solve for an improved single event location (red star and green error ellipse in Figure 5) with HYPOINVERSE [*Klein*, 2002]. The remaining (295) events were relocated with hypoDD, using differential traveltimes derived from both onset times and waveform cross correlation. This second step produced a cluster of 183 stable event locations. Traveltimes were updated relative to these new locations, and the main shock and the 183-event cluster were then relocated together using hypoDD. The results of this second relocation, composed of 181 events optimally clustered for the new data set, are shown in Figures 5–7.

3. Relocation Results

3.1. Apparent Fault Planes

[17] In contrast to the diffuse cloud of event locations reported in the INETER catalog (Figures 5 (left) and 6 (top)), the relocated hypocenters cluster into two planar features, plus a small number of less densely spaced events to the north (Figures 5 (right) and 6 (bottom)). The M_w 6.3 main event (red star), the M_w 5.3 foreshock (green star), and the majority of the aftershocks delineate a roughly vertical plane with a N60°E strike. This plane is roughly 16 km long (although perhaps as long as 21 km), and extends to 10 km depth. (To view the relocated hypocenters from a continuous range of azimuths, see Animation S1 in the auxiliary material.)[1] We interpret this plane as the fault that slipped during the M_w 6.3 earthquake.

[18] A second group of events relocated to the south of the first. These events also define a plane, albeit less sharply. The second plane strikes at N350°E–N355°E and is approximately 6 km long (yellow hypocenters in Animation S1). Seismicity on the second plane began on 3 August, 1604:30 UTC, roughly 5 h after the time of the main shock. (To

[1] Auxiliary materials are available in the HTML. doi:10.1029/2009GC002841.

15252027, 2010, 3, Downloaded from https://agupubs.onlinelibrary.wiley.com/doi/10.1029/2009GC002841 by Cochrane Costa Rica, Wiley Online Library on [21/07/2025]. See the Terms and Conditions (https://onlinelibrary.wiley.com/terms-and-conditions) on Wiley Online Library for rules of use; OA articles are governed by the applicable Creative Commons License

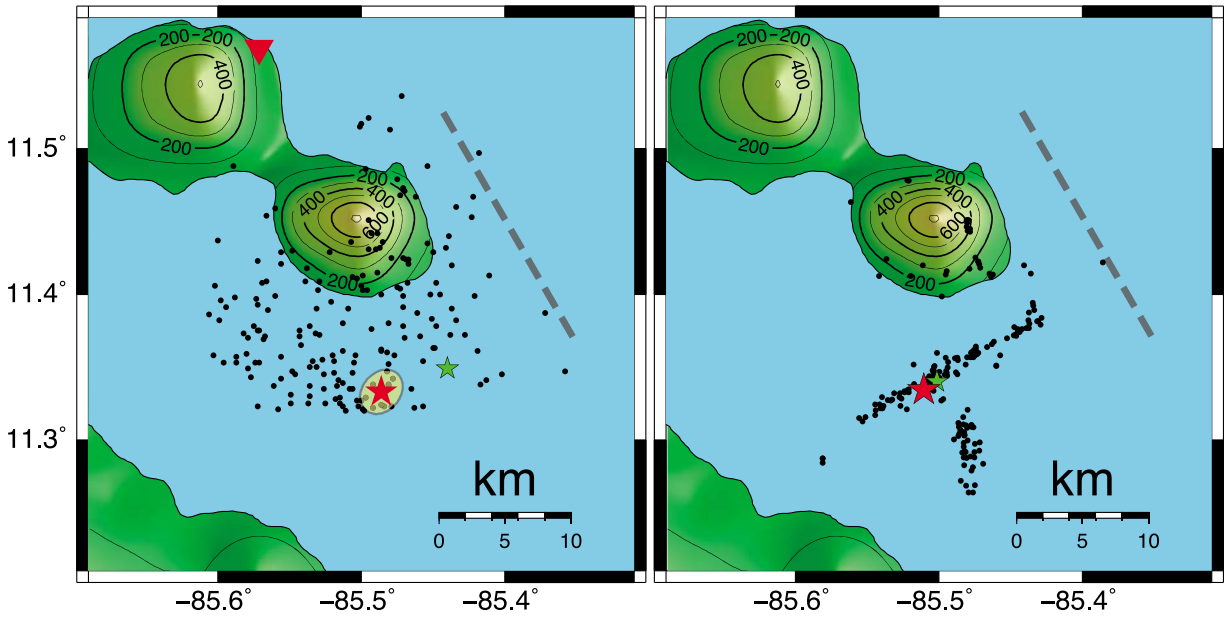

Figure 5. Map views of (left) initial and (right) double-difference relocated hypocenters. The green and red stars correspond to the M_w 5.3 and 6.3 fore and main shock, respectively. The dashed lines correspond to the profile in Figure 6. The initial hypocenters are INETER catalog locations except for the main shock, which was located separately using TUCAN *P* and *S* phase data (horizontal plane 95% confidence ellipse shown). The red inverted triangle represents the INETER catalog location of the main shock.

view the relocated hypocenters as a function of origin time, see Animation S2 in the auxiliary material.) We interpret this cluster as seismicity on a second fault plane that became active as a result of stress transferred from slip on the main shock fault plane.

[19] Scattered seismicity relocated to positions beneath and near Maderas volcano, the southern of the two volcanoes that comprise nearby Ometepe Island. However, these events did not begin until 4 August, 0544:00 UTC. No events from the INETER catalog relocated to positions beneath Concepción, the more northern Ometepe Island volcano that experienced minor eruptions during the time period for which events were relocated (July and August 2005).

3.2. Solution Convergence Characteristics

[20] Of the 296 INETER catalog events, hypoDD was able to define a cluster of 181 events that were sufficiently well connected into a pairwise network to admit double-difference relocation. The RMS residual for catalog-based differential traveltime data was 62 ms. For cross-correlation based differential traveltime data, the RMS residual was 77 ms. The largest RMS residual for any one station was 289 ms. As the relocation progressed, 16% of the original catalog-based differential traveltime data and 30% of the cross-correlation differential traveltime data were removed because they were classified as outliers. These losses are higher than the roughly 10% losses observed in the test cases described by

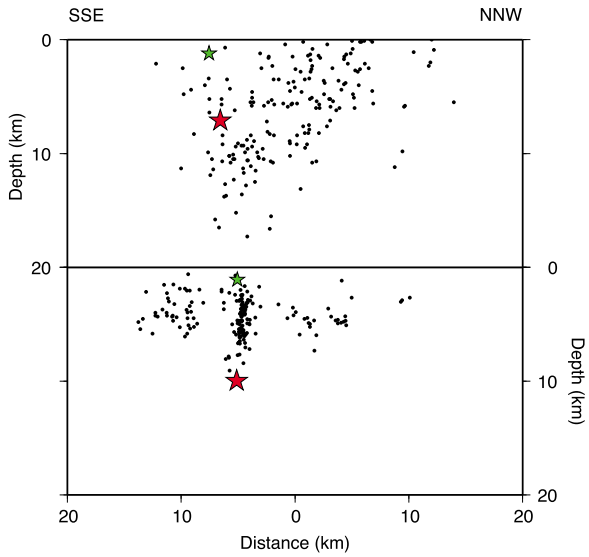

Figure 6. NNW striking depth profiles of the (top) initial and (bottom) double-difference relocated hypocenters shown in Figure 5. The profiles are oriented along the dashed lines in Figure 5. The green and red stars correspond to the M_w 5.3 and 6.3 fore and main shock, respectively.

15252027, 2010, 3, Downloaded from https://agupubs.onlinelibrary.wiley.com/doi/10.1029/2009GC002841 by Cochrane Costa Rica, Wiley Online Library on [21/07/2025]. See the Terms and Conditions (https://onlinelibrary.wiley.com/terms-and-conditions) on Wiley Online Library for rules of use; OA articles are governed by the applicable Creative Commons License

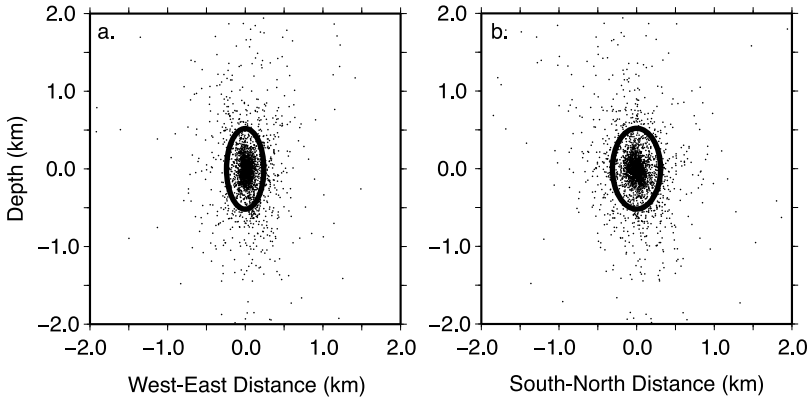

Figure 7. Results of the single-station jackknife resampling test shown in (a) west–east and (b) south–north depth profiles. Shifts in hypocenter location are plotted relative to the featured relocation. Ellipses illustrate the resulting 2σ bounds on hypocenter relative location uncertainty, based on the full data set of shifts from the jackknife test.

Waldhauser and Ellsworth [2000], and may be attributed to greater inaccuracy in the traveltime data coupled with less accurate starting locations.

4. Relocation Uncertainties

[21] While double-difference relocation excels at the relocation of events relative to each other, the absolute location of the solution can be strongly influenced by net inaccuracies in the event initial location model [*Waldhauser and Ellsworth*, 2000]. Here we examine both relative interevent errors within the solution and absolute location error of the solution as a whole.

4.1. Interevent Relative Location Uncertainty

[22] Because both initial locations and data weighting may affect solution structure, the reproducibility of the interevent locations was tested by systematically varying these relocation parameters. Use of the cluster centroid as an initial location (as opposed to individual event initial locations) produced essentially no effect on the interevent solution structure (with the exception of the main shock location, which is discussed below). The relocation was also carried out using only onset times or only waveform cross-correlation times. In these cases, individual event locations shifted slightly from their positions shown in Figures 5 and 6, but the position and orientation of the two apparent fault planes remained the same. In addition, to test the influence of the data weighting and the resulting removal of outlier data, the relocation was stopped before iteration 11, the point at which dynamic weighting is introduced. Interevent locations at this stage of the relocation strongly resemble the final solution, although the events that delineate the two apparent fault planes are considerably more diffuse. Based on these comparisons, the basic structure of the relative event locations appears to be robust.

[23] To test uncertainty in the location of the main shock, two alternative initial location models were also tested. In one case, the M_w 5.3 foreshock, the main shock, and two aftershocks immediately following the main shock were individually relocated relative to their INETER catalog locations with HYPOINVERSE and manually picked phase data. The rest of the events were relocated using hypoDD and the automatically picked onset times and waveform cross-correlation times. Using the new locations, all events were then relocated with hypoDD. Relative event locations were essentially unchanged, except that the main shock moved vertically upward by 100 m.

[24] In the second alternative, the M_w 5.3 foreshock, the main shock, and the same two aftershocks were relocated together with hypoDD, using manually picked phase data. The rest of the events were relocated with hypoDD and then all events were relocated with hypoDD. In this case, relative locations were again almost unchanged, except that the main shock shifted horizontally by 1.23 km to the NNW and shifted vertically upward by 2.98 km. Overall, relative locations are very stable, with the exception of the main shock. The variability in main shock location reflects the larger uncertainties in its traveltimes. As previously described, onset time picking for the main shock was impeded by emergent phases, and waveform cross correlation was inhibited by clipped waveforms. However, in all cases, the main shock lies

15252027, 2010, 3, Downloaded from https://agupubs.onlinelibrary.wiley.com/doi/10.1029/2009GC002841 by Cochrane Costa Rica, Wiley Online Library on [21/07/2025]. See the Terms and Conditions (https://onlinelibrary.wiley.com/terms-and-conditions) on Wiley Online Library for rules of use; OA articles are governed by the applicable Creative Commons License

within the N60°E striking plane of seismicity defined by the other events.

[25] In another experiment to test the stability of the relative locations, a shift of 0.10° in latitude and/or longitude was applied to all locations in the initial model. The pattern of seismicity exhibited negligible change under all such shifts, although the location of the entire cluster exhibited a net absolute translation. This result provides strong evidence for the stability of the interevent solution structure, while its implications for absolute location error are discussed in section 4.2.

[26] Finally, in an effort to determine the dependence of relative location stability on station distribution, a single-station jackknife bootstrap resampling test was implemented. In this test each of the 48 TUCAN stations in the input data set is "deleted" one at a time, and all data from that station are removed from the relocation. To ensure that cross-correlation and catalog differential traveltime data sets are comparable, except for the missing station in each of the 48 relocation trials, no dynamic weighting was employed. For each event, 48 shifts were calculated that describe its position in a trial with a missing station relative to its position from relocation with all stations.

[27] In general, the shifts are small, indicating relatively little dependence on individual stations (Figure 7). Based on our bootstrap resampling test, an estimated relative location 2σ error ellipse for our featured solution spans ±306 m in the W–E direction, ±394 m in the S–N direction, and ±661 m in the vertical direction. The root-mean-square (RMS) value of all bootstrap shifts in the horizontal plane is 225 m and the RMS vertical shift is 297 m. These RMS shifts are comparable to values found in tests of double-difference relocation with synthetic data using an event and station geometry broadly comparable to ours [*Lin and Shearer*, 2005]. However, for a small number of events in our data set, eliminating certain stations has a larger impact. The largest single shift within the horizontal plane is 3.83 km, while in the vertical plane it is 5.30 km.

4.2. Uncertainty in Absolute Locations

[28] Uncertainties in absolute event locations obtained with double-difference relocation are significant and much larger than uncertainties in relative locations [*Waldhauser and Ellsworth*, 2000; *Lin and Shearer*, 2005], and they are also more difficult to assess.

[29] Formal uncertainties associated with single event locations provide some insight. For example, the 95% confidence maximum horizontal error bound obtained from the HYPOINVERSE [*Klein*, 2002] relocation of the main shock from *P* and *S* onset times spans ±0.77 km in the horizontal plane (Figure 5 (left) shows full 95% horizontal error ellipse). These error ranges very likely underestimate the true uncertainty. HYPOINVERSE does not account for lateral heterogeneity, and its errors also do not reflect nonlinearity in the relocation inverse problem and raypath inaccuracy due to the assumed velocity structure. Looking at this question from a different angle, the hypoDD absolute location for the main shock falls within 3 km in the horizontal plane and 3 km vertically of its HYPOINVERSE location, suggesting a somewhat larger uncertainty.

[30] Like the tests described in the discussion of relative location error (section 4.1), a set of tests was also conducted to determine absolute location error. The entire set of initial event locations was translated by up to ±0.1° in latitude and/or longitude, resulting in a maximum shift of almost 16 km. Although shifts in relative locations were very slight during these tests, significant changes in differential traveltime misfits and solution behavior were observed, indicating some sensitivity to absolute location. For example, when initial locations were translated by 8 km or more to the NE, solution stability was degraded, resulting in some events relocating above ground and slight increases in traveltime misfit. For the largest shifts of 16 km, traveltime misfits increased significantly (by more than 30%) and in some cases a greater number of events relocated above ground.

[31] Loose bounds on the absolute location of the event cluster can also be obtained from observations of shaking and damage due to the M_w 6.3 main shock. In the days immediately following the 3 August 2005 main shock, INETER scientists conducted extensive intensity surveys of the surrounding region, including both Ometepe Island and mainland Nicaragua. Inferred intensities were greatest on Ometepe Island. The INETER field observations [*Morales and Tenorio*, 2005] integrated with standardized intensity scaling criteria [*Dengler and Dewey*, 1998] indicate that the southern tip of Ometepe Island experienced damage with MMI VIII, with the remainder of the southern half of the island corresponding to MMI VII and the northern half of the island corresponding to MMI VI. These damage patterns certainly suggest that the

15252027, 2010, 3, Downloaded from https://agupubs.onlinelibrary.wiley.com/doi/10.1029/2009GC002841 by Cochrane Costa Rica, Wiley Online Library on [21/07/2025]. See the Terms and Conditions (https://onlinelibrary.wiley.com/terms-and-conditions) on Wiley Online Library for rules of use; OA articles are governed by the applicable Creative Commons License

main shock was nearer to the southern tip of the island than points further north.

[32] In an attempt to define a rough location for the main shock, we turned to the 1972 M_w 6.2 Managua earthquake. The Managua event also occurred with left-lateral slip on a N45°E–N60°E trending vertical plane [*Brown et al.*, 1973; *LaFemina et al.*, 2002], and so is roughly analogous to the 3 August 2005 main shock in both magnitude and source mechanism. At a distance of roughly 7 km from the inferred 1972 epicenter, the distance from our event to the southern tip of Ometepe, *Algermissen et al.* [1974] observed damage consistent with MMI values of anywhere between VI and VIII depending on azimuth from the epicenter. Damage consistent with MMI VIII was observed to extend as far as 14 km from the Managua epicenter at some azimuths (specifically to the east along Lake Managua). A radius of 14 km from our event would cover a majority of the southern half of Ometepe. Making the risky assumption that a similar range of intensity versus distance scales can be used for the 2005 main shock, MMI values of VIII would be expected within 7 to 14 km of the epicenter. With this assumption, the location of the 2005 main shock in the preferred relocation solution is compatible with the intensity observations on Ometepe Island, but the true epicenter could also lie by as much as 7 km in a direction roughly to the south. An important caveat is that while the shallow geologies of the 1972 and 2005 epicentral regions are broadly similar (a mix of Quaternary volcanic rocks and volcaniclastic sediments), they differ in detail.

[33] Overall, the 3 km offset of the hypoDD main shock location from its HYPOINVERSE coordinates could be taken as a lower bound on absolute location uncertainty. This lower bound is somewhat larger than the roughly 2 km absolute location errors determined by *Lin and Shearer* [2005] in tests of double-difference relocation with synthetic data using an event and station geometry similar to ours. An upper bound is more difficult to assess, but a combination of the intensity measurements and the experiments with translating initial locations suggests that a value of roughly 7 km is reasonable.

5. Directivity Analysis

[34] Directivity analysis of the main shock waveforms confirms the N60°E fault plane identified by the relocation analysis. Since an earthquake rupture must propagate along the fault plane, the fault plane can be identified by estimating the rupture direction of the earthquake. We adapted the methodology of *Warren and Silver* [2006] to analyze the directivity of shallow earthquakes with regional data. Since this method was originally applied to deep earthquakes, we modified it to isolate the P wave by masking later arrivals. With this method, we measured the differential rupture duration (or stretching factor s) between each pair of seismograms using cross correlation. (If the rupture duration at station i is greater than that at station j, the stretching factor s_{ij} is greater than 1, and if the rupture duration at station j is greater than that at station i, the stretching factor s_{ij} is less than 1.) We used these measurements in a grid search over the entire focal sphere to determine the rupture vector that minimizes the misfit between the measured differences in duration and those predicted for unilateral rupture along that vector. We estimated errors in the rupture vector with bootstrap resampling [*Efron*, 1982]. For the bootstrap resampling, we repeated the directivity analysis 1000 times with randomly selected subsets of the stations recording the earthquake and drew confidence regions for the rupture vector that include 80% and 95% of the bootstrap-resampled rupture vectors. We compared the focal mechanism of the earthquake (taken from the Global Centroid Moment Tensor catalog) to the rupture vector confidence regions and noted the best fitting rupture direction on each nodal plane. To identify the fault plane, we compared how well rupture on each nodal plane can explain the observed differences in rupture duration.

[35] We analyzed the P wave directivity of the M_W 6.3 earthquake with vertical component seismograms recorded by 16 stations of the TUCAN network. The seismograms were deconvolved to displacement. Stations with clipped records, low signal-to-noise ratios, and later arrivals that interfered with the P waves were excluded. As shown in Figures 8 and 9, the N64°E striking nodal plane of the CMT provides a better fit by several measures. First, the 80% and 95% confidence regions for the rupture vector show that rupture propagated toward the east (Figures 8a and 8b). These confidence regions overlap the N64°E striking nodal plane but not the N334°E striking nodal plane. In addition, the alignment of seismograms relative to the best fitting rupture direction on the N64°E striking nodal plane shows a coherent increase in time between the two subevents with increasing angle from the rupture vector (Figure 9a). This pattern is

15252027, 2010, 3, Downloaded from https://agupubs.onlinelibrary.wiley.com/doi/10.1029/2009GC002841 by Cochrane Costa Rica, Wiley Online Library on [21/07/2025]. See the Terms and Conditions (https://onlinelibrary.wiley.com/terms-and-conditions) on Wiley Online Library for rules of use; OA articles are governed by the applicable Creative Commons License

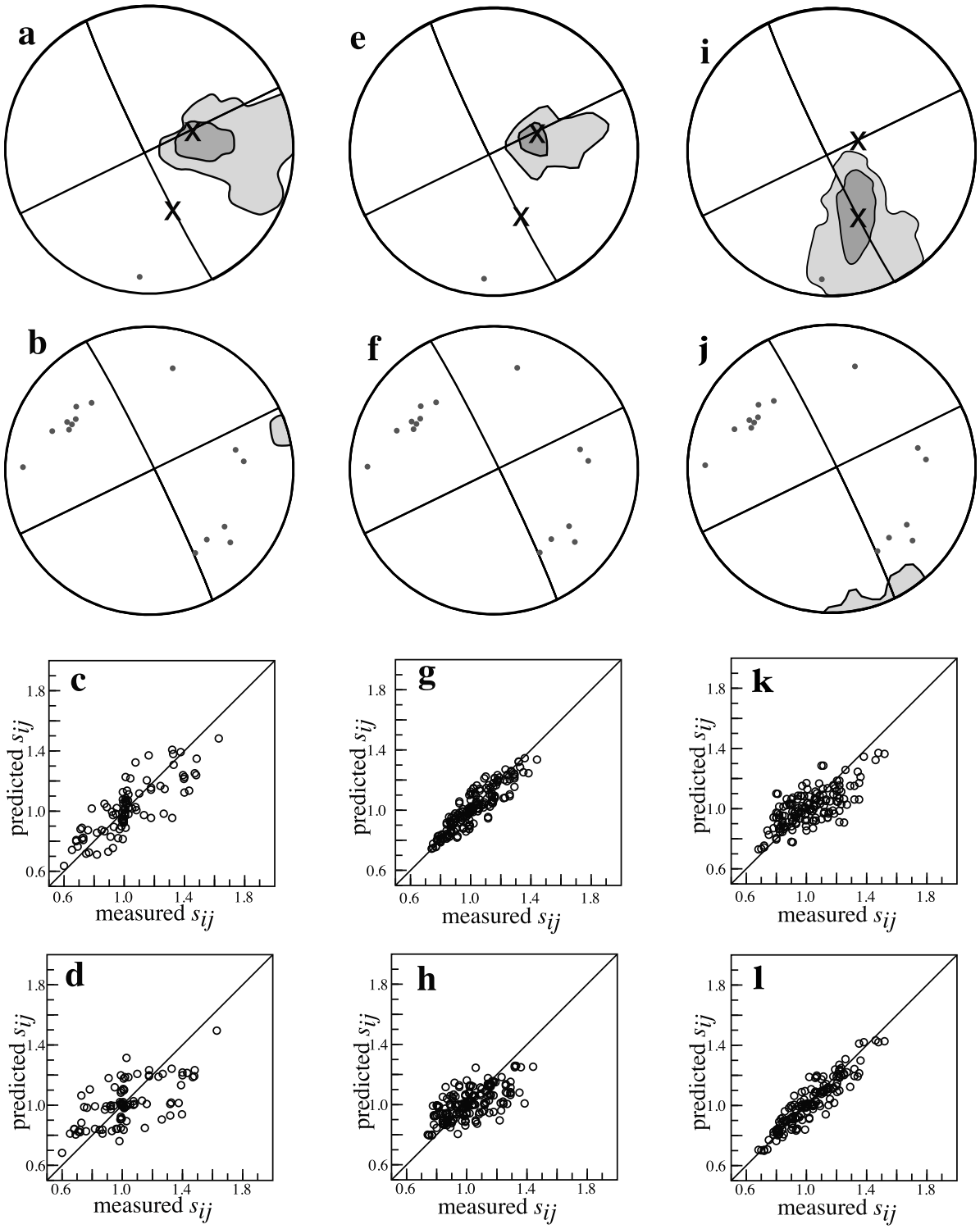

Figure 8. Directivity analyses for the main shock and synthetic earthquakes. The focal mechanism shows (a) upper and (b) lower hemisphere projections, with shading for the 80% (light gray) and 95% (dark gray) confidence regions for the rupture vector. Dots indicate takeoff vectors to stations, and crosses mark the best fitting rupture direction on each nodal plane. (c) Scatterplot comparing measured and predicted stretching factors for rupture on the N64°E striking nodal plane. (d) Scatterplot comparing measured and predicted stretching factors for rupture on the N334°E striking nodal plane. (e–h) Same as for Figures 8a–8d except for analysis of the synthetic seismograms for rupture on the N64°E striking nodal plane. (i–l) Same as for Figures 8a–8d except for analysis of the synthetic seismograms for rupture on the N334°E striking nodal plane.

15252027, 2010, 3, Downloaded from https://agupubs.onlinelibrary.wiley.com/doi/10.1029/2009GC002841 by Cochrane Costa Rica, Wiley Online Library on [21/07/2025]. See the Terms and Conditions (https://onlinelibrary.wiley.com/terms-and-conditions) on Wiley Online Library for rules of use; OA articles are governed by the applicable Creative Commons License

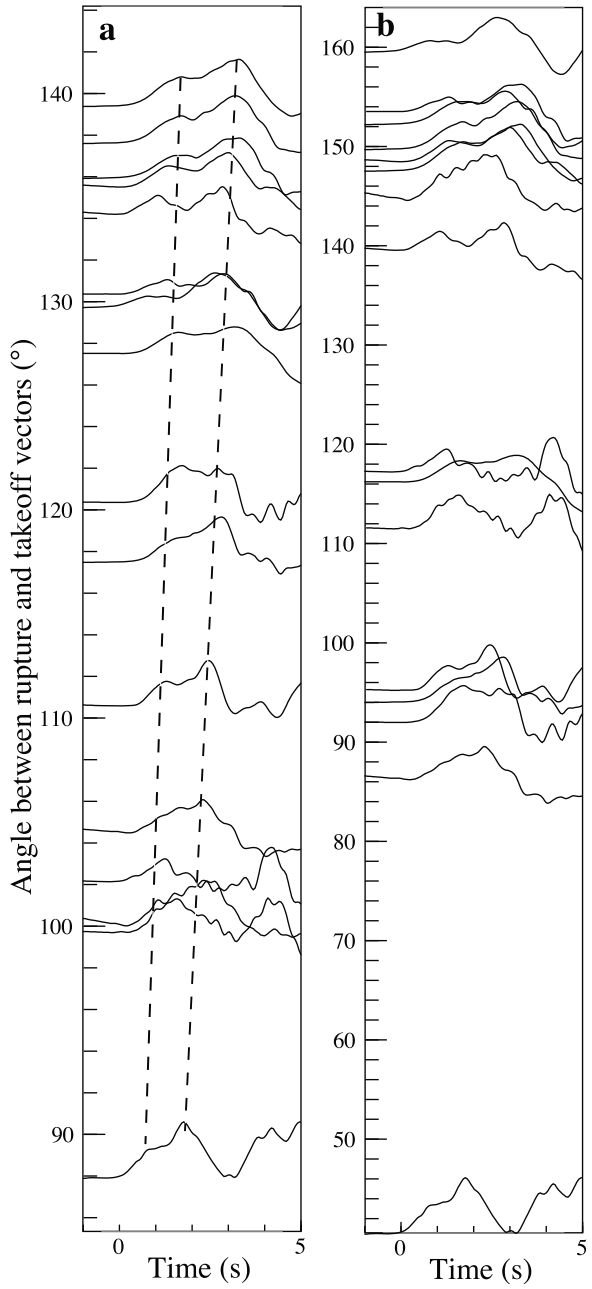

Figure 9. Seismograms aligned relative to the best fitting rupture direction on (a) the N64°E striking nodal plane and (b) the N334°E striking nodal plane. As indicated by the dashed lines, there is a coherent increase in the time between the two subevents for rupture on the N64°E striking nodal plane.

not seen for the N334°E striking nodal plane (Figure 9b). Further verification of the fault plane is found by comparing the misfit values for the two planes: the misfit is 0.57 for the N64°E striking nodal plane and 0.76 for the N334°E striking nodal plane (misfit values are normalized to range from zero to one). The difference in misfit can be seen qualitatively in the scatterplots, which show a higher correlation between measured and predicted stretching factors (s_{ij}'s) for the N64°E striking nodal plane (Figure 8c) than the N334°E striking nodal plane (Figure 8d).

[36] The directivity analysis was made using the main shock relocation as the earthquake location. The absolute location uncertainties described in section 4.2 would result in small changes to the takeoff vectors to the stations. This would only have a small effect on the determination of the rupture vector and would not affect our fault plane identification.

[37] The distribution of recording stations around the earthquake does affect the estimation of the rupture vector and associated confidence. Thus, we test how the station distribution affects their determination by generating synthetic seismograms for the best fitting rupture vector on each nodal plane and repeating the directivity analysis for them. The results for the synthetics for rupture on the N64°E striking nodal plane replicate the features seen in the real data: the 80% and 95% confidence regions are elongated toward the east (Figures 8e and 8f). On the other hand, synthetic rupture along the N334°E striking nodal plane leads to a different placement of the confidence regions and elongation to the south (Figures 8i and 8j). In addition, the scatterplots showing stretching factor correlations for the N64°E striking nodal plane synthetics (Figures 8g and 8h) more strongly resemble the observed stretching factor correlations (Figures 8c and 8d) than do the stretching factor correlations for the N334°E striking nodal plane synthetics (Figures 8k and 8l). Thus, the analysis of synthetics confirms the fault plane identification determined from the data.

6. Discussion

6.1. Implications for Models of Southern Nicaraguan Upper Plate Deformation

[38] The relocation and directivity analyses clearly show that rupture during the 3 August 2005 M_w 6.3 earthquake occurred on an N60°E trending fault plane. This result is consistent with left-lateral strike-slip motion on the N64°E vertical fault plane in the source mechanism determined by the Global Centroid Moment Tensor Project (http://www.globalcmt.org) [*Ekström*, 2007] (Figure 1). The M_w 5.3 foreshock has a similar source mechanism and also lies on the N60°E striking fault plane

15252027, 2010, 3, Downloaded from https://agupubs.onlinelibrary.wiley.com/doi/10.1029/2009GC002841 by Cochrane Costa Rica, Wiley Online Library on [21/07/2025]. See the Terms and Conditions (https://onlinelibrary.wiley.com/terms-and-conditions) on Wiley Online Library for rules of use; OA articles are governed by the applicable Creative Commons License

delineated by the relocated hypocenters, suggesting that this event also corresponds to left-lateral strike-slip motion. These results are consistent with the bookshelf faulting model of *LaFemina et al.* [2002] for deformation within the Nicaraguan fore arc and arc. In particular, they show that a key feature of the bookshelf fault model, left-lateral slip on roughly arc-normal strike-slip faults, occurs in Lake Nicaragua, a region where prior evidence was weak. The recent seismic reflection study of *Funk et al.* [2009], however, did not image a N60°E trending fault plane that coincides with the relocated event sequence, despite multiple survey lines in the area of Lake Nicaragua south of Ometepe Island, nor did they observe a system of NE striking strike-slip faults elsewhere within Lake Nicaragua. As previously mentioned, these results led *Funk et al.* [2009] to conclude that fore-arc sliver transport occurs by right-lateral strike-slip motion on faults that strike roughly parallel to the arc. However, the lack of vertical motion on the N60°E trending fault delineated by the relocation analysis would likely make it more difficult to observe using reflection methods than the normal faults observed by *Funk et al.* [2009] in Lakes Nicaragua and Managua and the Gulf of Fonseca.

6.2. Average Slip

[39] Assuming that the aftershocks define the area of the fault plane that ruptured during the main shock, average slip on the fault plane can be roughly estimated. The fault plane area is 8–12 km in depth by 14–21 km in length. The seismic moment reported for the main shock is 3.01e+25 dyn cm. For a shear modulus of 3e+11 dyn/cm^2, slip of 40–90 cm is implied. This slip value is a reminder that one earthquake only represents a small amount of displacement in a single location. While the 3 August 2005 earthquake is consistent with bookshelf faulting, it could also fit a variety of other deformation patterns.

6.3. Activation of a Second Fault Plane

[40] While the bulk of the events in our sequence relocated within the N60°E striking plane, roughly 5 h after the main shock a second plane became active (Animation S2). As described in section 3.1, this secondary plane is also roughly vertical and strikes N350°E to N355°E (Figure 5 and Animation S1). First-motion polarities from the largest event on the secondary plane are consistent with a strike-slip focal mechanism similar to those of the fore and main shocks on the primary plane, although the precise orientation of the fault plane cannot be determined. This result suggests that the secondary cluster represents right-lateral strike-slip motion on a N350°E to N355°E trending fault plane. The timing of initiation of seismicity on this plane suggests that it was activated by the rupture of the main shock fault plane, either by dynamic triggering due to large amplitude seismic energy associated with the main shock [e.g., *Felzer and Brodsky*, 2006], or by Coulomb stress changes due to the left-lateral main shock slip [e.g., *King et al.*, 1994]. In addition, while *Funk et al.* [2009] failed to image the main shock fault plane, they did infer a series of NW to NNW trending normal faults, which they termed the San Ramon Fault Zone, in the vicinity of our secondary feature. The San Ramon normal faults dip to the NE, whereas the aftershocks suggest a vertical to slightly SW dip for the secondary fault plane found in this study. However, the dip of the secondary fault plane is not well constrained. Thus, it is possible that rupture of the main shock fault plane induced right-lateral strike-slip motion on one or more of the normal faults in the San Ramon Fault Zone.

6.4. Correlation With Volcanic Activity

[41] Concepción volcano, the more northwestern of the two volcanoes that comprise Ometepe Island, experienced a small ash eruption on 28 July 2005, 6 days before the start of the earthquake sequence, and intermittent explosions of gas and ash continued into November 2005. Because of the rough temporal correlation between the beginning of this eruptive episode and the clearly tectonic earthquake sequence, we considered the possibility of a causal link between the two. An excellent example of causal behavior is the 1999 eruption of Cerro Negro volcano in northern Nicaragua that appears to have been triggered by Coulomb stress changes produced by three M_w 5.1–5.2 earthquakes that preceded the eruption by less than 12 h [*LaFemina et al.*, 2004; *Díez et al.*, 2005]. These earthquakes also produced a significant aftershock sequence whose distribution is consistent with predicted Coulomb stress [*Díez et al.*, 2005]. An obvious difference between this example and the July–August eruption and earthquake sequence is that, in the latter case, the largest events followed the initial eruption and the time delay was significantly larger. However, as mentioned previously, volcano to earthquake triggering has been postulated in other regions [e.g., *Nostro et al.*, 1998], and other events exhibiting a loose temporal correlation have been observed in southern Nicaragua (e.g., the

15252027, 2010, 3, Downloaded from https://agupubs.onlinelibrary.wiley.com/doi/10.1029/2009GC002841 by Cochrane Costa Rica, Wiley Online Library on [21/07/2025]. See the Terms and Conditions (https://onlinelibrary.wiley.com/terms-and-conditions) on Wiley Online Library for rules of use; OA articles are governed by the applicable Creative Commons License

16 December 1985 M_w 6.1 Ochomogo earthquake and December 1985 to April 1986 volcanic activity at Concepción).

[42] Nonetheless, no clear evidence exists that the Concepción eruption and tectonic earthquakes associated with the 3 August 2005 main shock were linked by changes in crustal stress. First, the events included in the relocation analysis include all events in the INETER catalog for July as well as August 2005 that fell within a 0.5° × 0.5° box centered on the main shock location. Therefore, if significant foreshocks of the 3 August 2005 M_w 6.3 event preceded and possibly aided in triggering the Concepción eruption, they should have appeared in our analysis, and none exist. Second, the 2005 main shock fault plane is significantly offset in space from the volcano, more than 15 km away from Concepción assuming our preferred location model, and at least 8 km allowing for the outer limit of absolute location error. Therefore, for the volcano to have a role in triggering the earthquakes, significant stresses would need to be transmitted over distances of at least 8 and more likely 15 km. In contrast, in the case of the 1999 Cerro Negro eruption, the M_w 5.1–5.2 earthquakes that appear to have triggered the eruption were located within 1–2 km of the volcano. Two-way coupling between volcanic eruptions and earthquakes has been inferred over longer length scales, but the causative eruptions were much larger [*Nostro et al.*, 1998]. Finally, if the Concepción eruption did significantly alter crustal stress, some small tectonic earthquakes might be expected within a few kilometers of the volcano. Volcanic tremor and some very small volcanic earthquakes were recorded at an INETER station on Ometepe Island just to the north of Concepción (http://www.volcano.si.edu/reports/bulletin). However, no earthquakes in our analysis (i.e., earthquakes large enough to appear in the INETER catalog) relocated to positions beneath Concepción, and the small number of events that relocated to positions beneath Maderas volcano did not begin until more than 16 h after the main shock.

[43] Based on these observations, we lean toward the interpretation that the close timing of the Concepción eruption and the August 2005 earthquake sequence is a coincidence. However, we cannot rule out the possibility that some unobserved transfer of stress did occur between the volcano and fault zone or vice versa. An event of similar size (M_w 6.1) and source mechanism that occurred in Costa Rica on 8 January 2009 provides another example where links between earthquake and volcanic activity are unclear. This earthquake was located in between Poas and Barva volcanoes at distances of less than 5 km from either volcano, and no changes in volcanic activity were observed either before or after the earthquake.

7. Conclusions

[44] Double-difference relocation of the August 2005 main shock and foreshock/aftershock sequence delineates a roughly vertical fault that strikes at N60°E. Directivity analysis of main shock waveforms confirms this surface as the main shock fault plane. These results, coupled with the main shock source mechanism, indicate left-lateral slip on a fault plane oriented roughly normal to the arc. This conclusion is consistent with the hypothesis that upper plate deformation in the Nicaraguan arc is dominated by bookshelf faulting, although bookshelf faulting is not uniquely required.

[45] Relocated hypocenters also define a second roughly vertical plane of seismicity that lies to the south of the main shock fault and strikes N350°E–N355°E. Polarity data indicate that right-lateral slip is the most likely sense of motion on this secondary fault. Seismicity on this surface began 5 h after the main shock, suggesting that it was activated by dynamic triggering or Coulomb stress changes produced by slip on the main shock fault plane.

[46] Although Concepción volcano erupted 6 days prior to the earthquake sequence, local seismicity does not clearly point to a transfer of crustal stress that links these events. No events spatially correlated with this earthquake sequence were detected within the month prior to the eruption of Concepción, suggesting that the eruption was not triggered at short time scales by stress transfer from slip on this fault. No earthquakes in our analysis relocated beneath Concepción either before or after the eruption. If the eruption was able to perturb crustal stress to the point where it could influence tectonic activity on the main shock fault, at distances of at least 8 km and probably more than 15 km from the volcano, it must have done so without producing significant seismicity more local to the volcano.

Acknowledgments

[47] Thanks to Virginia Tenorio, Pedro Pérez, Allan Morales, Catherine Rychert, Ellen Syracuse, Laura MacKenzie, David Abt, Mariela Salas de la Cruz, Alexis Walker, Gustavo Reyes, and Tim Parker for their work on the TUCAN Broadband Seismic Experiment and to the IRIS/PASSCAL program for

15252027, 2010, 3, Downloaded from https://agupubs.onlinelibrary.wiley.com/doi/10.1029/2009GC002841 by Cochrane Costa Rica, Wiley Online Library on [21/07/2025]. See the Terms and Conditions (https://onlinelibrary.wiley.com/terms-and-conditions) on Wiley Online Library for rules of use; OA articles are governed by the applicable Creative Commons License

the seismometers. Thanks also to Peter LaFemina and Robert McCaffrey for very helpful reviews. This research and the TUCAN Seismic Experiment were supported by the NSF MARGINS program through awards OCE-0203607, OCE-0203650, and OCE-0646667.

References

Algermissen, S. T., J. W. Dewey, C. J. Langer, and W. H. Dillinger (1974), The Managua, Nicaragua, earthquake of December 23, 1972: Location, focal mechanism, and intensity distribution, *Bull. Seismol. Soc. Am.*, *64*, 993–1004.

Brown, R. D., P. L. Ward, and G. Plafker (1973), Geologic and seismologic aspects of the Managua, Nicaragua, earthquakes of December 23, 1972, *U.S. Geol. Surv. Prof. Pap., 838*.

Cailleau, B., P. C. LaFemina, and T. H. Dixon (2007), Stress accumulation between volcanoes: An explanation for intra-arc earthquakes in Nicaragua?, *Geophys. J. Int.*, *169*, 1132–1138, doi:10.1111/j.1365-246X.2007.03353.x.

Carr, M. J., and R. E. Stoiber (1977), Geologic setting of some destructive earthquakes in Central America, *Geol. Soc. Am. Bull.*, *88*, 151–156, doi:10.1130/0016-7606(1977)88<151:GSOSDE>2.0.CO;2.

Cowan, H., M. N. Machette, X. Amador, K. S. Morgan, R. L. Dart, and L. Bradley (2000), Map and database of Quaternary faults in the vicinity of Managua, Nicaragua, *U.S. Geol. Surv. Open File Rep., 00–437*.

DeMets, C. (2001), A new estimate for present-day Cocos-Caribbean plate motion: Implications for slip along the Central American volcanic arc, *Geophys. Res. Lett.*, *28*, 4043–4046, doi:10.1029/2001GL013518.

Dengler, L. A., and J. W. Dewey (1998), An intensity survey of households affected by the Northridge, California, earthquake of 17 January, 1994, *Bull. Seismol. Soc. Am.*, *88*, 441–462.

Díez, M., P. C. LaFemina, C. B. Connor, W. Strauch, and V. Tenorio (2005), Evidence for static stress changes triggering the 1999 eruption of Cerro Negro Volcano, Nicaragua and regional aftershock sequences, *Geophys. Res. Lett.*, *32*, L04309, doi:10.1029/2004GL021788.

Earle, P. S., and P. M. Shearer (1994), Characterization of global seismograms using an automatic picking algorithm, *Bull. Seismol. Soc. Am.*, *84*, 366–376.

Efron, B. (1982), *The Jackknife, the Bootstrap and Other Resampling Plans*, *CBMS-NSF Reg. Conf. Ser. Appl. Math*, vol. 38, Soc. for Ind. and Appl. Math, Philadelphia, Pa.

Ekström, G. (2007), Global seismicity: Results from systematic waveform analyses, 1976–2005, in *Treatise on Geophysics*, vol. 4, *Earthquake Seismology*, edited by H. Kanamori, pp. 473–481, Elsevier, Amsterdam.

Ekström, G., and E. Engdahl (1989), Earthquake source parameters and stress distribution in the Adak Island Region of the central Aleutian Islands, Alaska, *J. Geophys. Res.*, *94*, 15,499–15,519, doi:10.1029/JB094iB11p15499.

Felzer, K. R., and E. E. Brodsky (2006), Decay of aftershock density with distance indicates triggering by dynamic stress, *Nature*, *441*, 735–738, doi:10.1038/nature04799.

Fitch, T. (1972), Plate convergence, transcurrent faults, and internal deformation adjacent to Southeast Asia and the western Pacific, *J. Geophys. Res.*, *77*, 4432–4460, doi:10.1029/JB077i023p04432.

Funk, J., P. Mann, K. McIntosh, and J. Stephens (2009), Cenozoic tectonics of the Nicaraguan depression, Nicaragua, and Median Trough, El Salvador, based on seismic-reflection profiling and remote-sensing data, *Geol. Soc. Am. Bull.*, *121*, 1491–1521, doi:10.1130/B26428.1.

Iinuma, T., M. Protti, K. Obana, V. Gonzalez, R. van der Laat, T. Kato, S. Miyasaki, Y. Kaneda, and E. Hernandez (2004), Inter-plate coupling in the Nicoya Peninsula, Costa Rica, as deduced from a trans-peninsula GPS experiment, *Earth Planet. Sci. Lett.*, *223*, 203–212, doi:10.1016/j.epsl.2004.04.016.

King, G. C. P., R. S. Stein, and J. Lin (1994), Static stress changes and the triggering of earthquakes, *Bull. Seismol. Soc. Am.*, *84*, 935–953.

Klein, F. W. (2002), User's guide to HYPOINVERSE-2000, a Fortran program to solve for earthquake locations and magnitudes (version 4/2002), *U.S. Geol. Surv. Open File Rep., 02–171*.

LaFemina, P. C., T. H. Dixon, and W. Strauch (2002), Bookshelf faulting in Nicaragua, *Geology*, *30*, 751–754, doi:10.1130/0091-7613(2002)030<0751:BFIN>2.0.CO;2.

LaFemina, P. C., C. B. Connor, B. E. Hill, W. Strauch, and J. A. Saballos (2004), Magma-tectonic interactions in Nicaragua: The 1999 seismic swarm and eruption of Cerro Negro volcano, *J. Volcanol. Geotherm. Res.*, *137*, 187–199, doi:10.1016/j.jvolgeores.2004.05.006.

LaFemina, P., T. H. Dixon, R. Govers, E. Norabuena, H. Turner, A. Saballos, G. Mattioli, M. Protti, and W. Strauch (2009), Fore-arc motion and Cocos Ridge collision in Central America, *Geochem. Geophys. Geosyst.*, *10*, Q05S14, doi:10.1029/2008GC002181.

Lin, G., and P. Shearer (2005), Tests of relative earthquake relocation techniques using synthetic data, *J. Geophys. Res.*, *110*, B04304, doi:10.1029/2004JB003380.

Lundgren, P., M. Protti, A. Donnellan, M. Heflin, E. Hernandez, and D. Jefferson (1999), Seismic cycle and plate margin deformation in Costa Rica: GPS observations from 1994 to 1997, *J. Geophys. Res.*, *104*, 28,915–28,926, doi:10.1029/1999JB900283.

Marshall, J. S., D. M. Fisher, and T. W. Gardner (2000), Central Costa Rica deformed belt: Kinematics of diffuse faulting across the Panama block, *Tectonics*, *19*, 468–492, doi:10.1029/1999TC001136.

Martínez-Díaz, J. J., J. A. Álvarez-Gómez, B. Benito, and D. Hernández (2004), Triggering of destructive earthquakes in El Salvador, *Geology*, *32*, 65–68, doi:10.1130/G20089.1.

McCaffrey, R. (1992), Oblique plate convergence, slip vectors, and forearc deformation, *J. Geophys. Res.*, *97*, 8905–8915, doi:10.1029/92JB00483.

McCaffrey, R. (1996), Estimates of modern arc-parallel strain rates in fore arcs, *Geology*, *24*, 27–30, doi:10.1130/0091-7613(1996)024<0027:EOMAPS>2.3.CO;2.

McCaffrey, R., P. C. Zwick, Y. Bock, L. Prawirodirdjo, J. F. Genrich, C. W. Stevens, S. S. O. Puntodewo, and C. Subarya (2000), Strain partitioning during oblique plate convergence in northern Sumatra: Geodetic and seismologic constraints and numerical modeling, *J. Geophys. Res.*, *105*, 28,363–28,376, doi:10.1029/1999JB900362.

Morales, A., and V. Tenorio (2005), Encuesta Macrosísmica del Terremoto magnitud 5.7 del 3 de agosto, 6:03 am, *Mon. Geophys. Bull., Sismos y Volcanes de Nicaragua*, Inst. Nicaragüense de Estud. Territ., Managua, Aug. (Available at http://www.ineter.gob.ni/geofisica/boletin/2005/08/eventos-especiales-encuesta-lago050803.htm)

Norabuena, E., et al. (2004), Geodetic and seismic constraints on some seismogenic zone processes in Costa Rica, *J. Geophys. Res.*, *109*, B11403, doi:10.1029/2003JB002931.

Nostro, C., R. Stein, M. Cocco, M. Belardinelli, and W. Marzocchi (1998), Two-way coupling between Vesuvius eruptions and

15252027, 2010, 3, Downloaded from https://agupubs.onlinelibrary.wiley.com/doi/10.1029/2009GC002841 by Cochrane Costa Rica, Wiley Online Library on [21/07/2025]. See the Terms and Conditions (https://onlinelibrary.wiley.com/terms-and-conditions) on Wiley Online Library for rules of use; OA articles are governed by the applicable Creative Commons License

southern Apennine earthquakes, Italy, by elastic stress transfer, *J. Geophys. Res.*, *103*(B10), 24,487–24,504, doi:10.1029/98JB00902.

Paige, C. C., and M. A. Saunders (1982), LSQR: An algorithm for sparse linear equations and sparse least squares, *Trans. Math. Software*, *8*, 43–71, doi:10.1145/355984.355989.

Phipps Morgan, J., C. R. Ranero, and P. Vannucchi (2008), Intra-arc extension in Central America: Links between plate motions, tectonics, volcanism, and geochemistry, *Earth Planet. Sci. Lett.*, *272*, 365–371, doi:10.1016/j.epsl.2008.05.004.

Red Sismológica Nacional (2009), El terremoto de Cinchona del jueves 8 de enero de 2009, *Rev. Geol. Am. Cent.*, *40*, 91–95.

Sieh, K., and D. Natawidjaja (2000), Neotectonics of the Sumatran fault, Indonesia, *J. Geophys. Res.*, *105*(B12), 28,295–28,326, doi:10.1029/2000JB900120.

Turner, H. L., III, P. LaFemina, A. Saballos, G. S. Mattioli, P. E. Jansma, and T. Dixon (2007), Kinematics of the Nicaraguan forearc from GPS geodesy, *Geophys. Res. Lett.*, *34*, L02302, doi:10.1029/2006GL027586.

van Wyk de Vries, B. (1993), Tectonics and magma evolution of Nicaraguan volcanic systems, Ph.D. thesis, Open Univ., Milton Keynes, U. K.

Waldhauser, F. (2001), hypoDD: A program to compute double-difference hypocenter locations (version 3/2001), *U.S. Geol. Surv. Open File Rep., 01–113*.

Waldhauser, F., and W. L. Ellsworth (2000), A double-difference earthquake location algorithm: Method and application to the northern Hayward Fault, CA, *Bull. Seismol. Soc. Am.*, *90*, 1353–1368, doi:10.1785/0120000006.

Warren, L. M., and P. G. Silver (2006), Measurement of differential rupture durations as constraints on the source finiteness of deep earthquakes, *J. Geophys. Res.*, *111*, B06304, doi:10.1029/2005JB004001.

Weinberg, R. F. (1992), Neotectonic development of western Nicaragua, *Tectonics*, *11*, 1010–1017, doi:10.1029/92TC00859.

White, R. A. (1991), Tectonic implications of upper-crustal seismicity in Central America, in *Neotectonics of North America*, vol. 1, edited by D. B. Slemmons et al., pp. 323–338, Geol. Soc. of Am., Boulder, Colo.

White, R. A., and D. H. Harlow (1993), Destructive upper-crustal earthquakes of Central America since 1900, *Bull. Seismol. Soc. Am.*, *38*, 1115–1142.

15252027, 2010, 3, Downloaded from https://agupubs.onlinelibrary.wiley.com/doi/10.1029/2009GC002841 by Cochrane Costa Rica, Wiley Online Library on [21/07/2025]. See the Terms and Conditions (https://onlinelibrary.wiley.com/terms-and-conditions) on Wiley Online Library for rules of use; OA articles are governed by the applicable Creative Commons License